Article:
Nawilaijaroen, Yonlada, Rocliffe, Holly R., Austin-Williams, Shani et al. (2025) MC1R determines healing outcomes in acute and chronic cutaneous wounds. Proceedings of the National Academy of Sciences of the United States of America. e2503308122. ISSN: 1091-6490

https://doi.org/10.1073/pnas.2503308122

PNAS RESEARCH ARTICLE | IMMUNOLOGY AND INFLAMMATION OPEN ACCESS

MC1R determines healing outcomes in acute and chronic cutaneous wounds

Yonlada Nawilaijaroen[a], Holly R. Rocliffe[a,1], Shani Austin-Williams[b,1], Georgios Krilis[c,1], Charlotte Dawson[a], Pruistinne Harijanto[a], Antonella Pellicoro[a], Kanheng Zhou[d], Yubo Ji[d], Connor A. Bain[e], Alastair M. Kilpatrick[f], Yuhang Chen[e], Asok Biswas[g], Shareen Forbes[c], Michael Crichton[e], Zhihong Huang[d], Stuart J. Forbes[f], Andrea Caporali[c], and Jenna L. Cash[a,2]

Affiliations are included on p. 10.

Edited by Yizhou Dong, Icahn School of Medicine at Mount Sinai, New York, NY; received February 13, 2025; accepted October 7, 2025 by Editorial Board Member Carl F. Nathan

Chronic wounds (CWs) represent a major clinical challenge, characterized by persistent inflammation and failed repair. While proresolving pathways are known to regulate inflammatory responses, their potential dysfunction in CWs remains unexplored. Here, we identify dysregulation of the pro-opiomelanocortin-melanocortin 1 receptor (POMC–MC1R) axis as a common feature across pressure ulcers, venous ulcers, and diabetic ulcers. Using MC1Re/e mice lacking functional MC1R, we demonstrate impaired wound healing marked by delayed reepithelialization and increased neutrophil extracellular traps—pathological features observed in human CWs. To investigate MC1R's therapeutic potential, we developed a new murine CW model that replicates human pathology, presenting as nonhealing, exudate-rich ulcers. Topical application of the MC1R-selective agonist BMS-470539 restored healing by reducing exudate production, stimulating vascularization, and enabling reepithelialization. The critical role of MC1R was further evidenced by MC1Re/e mice, which developed more severe ulcers with excessive exudate and NETosis. In acute wound studies, we found that topical MC1R agonist enhanced wound bed perfusion and lymphatic drainage through increased angiogenesis and lymphangiogenesis and reduced scarring by modulating fibroblast phenotype. Together, these findings establish the MC1R/POMC axis as a fundamental regulator of skin repair and identify promising therapeutic strategies to drive healing.

wound | inflammation | skin | chronic | resolution

Significance

Chronic wounds (CWs) are a major healthcare challenge, characterized by persistent inflammation that fails to resolve naturally. We found that dysregulation of the proresolving POMC–MC1R pathway is a common feature across different types of CWs including diabetic ulcers and pressure sores. Using a mouse model that replicates human CWs, we demonstrated that targeting MC1R with a topical drug promotes healing by improving blood vessel formation, reducing neutrophil recruitment and NET formation to restore tissue repair. By identifying MC1R as a central regulator of wound repair, we provide a promising therapeutic strategy that could benefit millions of patients suffering from nonhealing wounds.

Skin is a fascinating and complex barrier organ composed of multiple layers and cell types that are functionally distinct. Skin repair following injury involves four overlapping, sequential phases: coagulation, inflammation, proliferation/migration, and remodeling, culminating in scar formation (1, 2). In acute wounds, both the magnitude and duration of the inflammatory response correlate with the severity of scarring, while chronic wounds (CWs) are characterized by persistent, nonresolving inflammation (2, 3). Proresolving pathways, including Annexin A1/FPR2, Chemerin/ChemR23, and POMC/MC1R signaling, are known to regulate inflammatory resolution through anti-inflammatory and phagocytic mechanisms, though their broader roles in tissue repair and healing failure are only beginning to be understood (4–8).

CWs, including venous leg ulcers (VLU), diabetic foot ulcers (DFU), and pressure ulcers (PU), fail to effectively execute a healing response and become "stuck" in a chronically inflamed state. They represent a global and escalating health burden due to a sharp rise in worldwide incidence of key comorbidities, including diabetes, obesity, and advanced age (3, 9). CW complications include infection, amputation, sepsis, and death, imposing substantial morbidity and mortality on individuals and healthcare systems. This burden equates to approximately £8 billion pa spent by the UK National Health Service (NHS) on 3.8 million wounds (10–12) and a cost projection of 28 to 97 billion on 8.2 million Medicare beneficiaries with wounds (13).

The melanocortin system, particularly Melanocortin 1 Receptor (MC1R), represents an understudied pathway in wound repair. While MC1R is known for its roles in pigmentation and UV protection, it is also expressed on multiple cell types involved in wound repair (14, 15). Previous studies have explored MC1R's anti-inflammatory properties in other contexts, such as arthritis models, where MC1R agonism can reduce immune cell recruitment and activation (4, 16).

Here, we reveal previously unrecognized functions of MC1R in wound repair through both genetic and pharmacological approaches. Using MC1Re/e mice and a selective MC1R agonist, we demonstrate that MC1R is required for efficient healing and identify its roles in

Author contributions: Z.H., A.C., and J.L.C. designed research; Y.N., H.R.R., S.A.-W., G.K., C.D., P.H., A.P., K.Z., Y.J., C.A.B., A.M.K., Y.C., A.B., M.C., A.C., and J.L.C. performed research; K.Z., Y.J., C.A.B., Y.C., S.J.F., M.C., and Z.H. contributed new reagents/analytic tools; Y.N., H.R.R., S.A.-W., G.K., A.P., K.Z., Y.J., C.A.B., A.M.K., Y.C., M.C., A.C., and J.L.C. analyzed data; S.F. provided expertise on diabetes; S.J.F. supervision of AMK; and Y.N., C.D., C.A.B., and J.L.C. wrote the paper.

Competing interest statement: Jenna Cash has acted as a consultant for BioTherapy Services. All other authors declare no competing interests.

This article is a PNAS Direct Submission. Y.D. is a guest editor invited by the Editorial Board.

[1]H.R.R., S.A.-W., and G.K. contributed equally to this work.

[2]To whom correspondence may be addressed. Email: Jenna.cash@ed.ac.uk.

This article contains supporting information online at https://www.pnas.org/lookup/suppl/doi:10.1073/pnas.2503308122/-/DCSupplemental.

Published November 11, 2025.

promoting angiogenesis, lymphangiogenesis, and appropriate matrix deposition. Utilizing single-cell RNA sequencing data from healthy, healing, and nonhealing DFU, we reveal marked dysregulation of proresolving pathways in human nonhealing wounds. Multiplex immunofluorescence confirmed MC1R expression in blood vessels, keratinocytes, and fibroblasts, alongside reduced ligand POMC expression across three CW categories. We successfully develop a reproducible and humane animal model of CWs that recapitulates key pathological features of the human condition. Using this model, we show that topical MC1R agonist treatment can rescue stalled healing, whereas animals lacking functional MC1R exhibit more severe CWs. Notably, MC1R agonist also enhanced acute wound repair by improving wound vascularization and reducing scarring. These findings collectively indicate that defects in proresolving pathways contribute to the pathophysiology of chronic nonhealing wounds, highlighting MC1R as a promising therapeutic target.

Results

Proresolving Pathways Including the POMC–MC1R Axis Are Dysregulated in Human CWs. Tissue damage triggers an acute inflammatory response that is short-lived and self-resolving in nature, however chronic nonhealing wounds exhibit sustained nonresolving inflammation. Proresolving mediators and their cognate receptors (proresolving pathways) function to control inflammatory resolution (5, 17), however their regulation in CWs remains unexplored.

Here, we interrogated a published scRNAseq dataset of healthy skin, DFU that healed within 12 wk (Healing DFU) and those that failed to heal within 12 wk (nonhealing DFU, (18). We examined three proresolving pathways, *ANXA1/FPR2* (Annexin A1/FPR2), *RARRES2/CMKLR1* (Chemerin/ChemR23), and *POMC/MC1R*, as these represent paradigmatic mechanisms of inflammation resolution (Fig. 1 *A* and *B* and *SI Appendix*, Fig. S1*A*). CellChat analysis was used to infer cell–cell communication networks by quantifying ligand–receptor interactions and their relative strengths across different cell populations (19). Strikingly, we reveal that each of these signaling pathways shows increased interaction strength in healing DFU compared to healthy skin, while nonhealing DFU typically exhibited interaction strengths even lower than healthy skin (Fig. 1 *A* and *B* and *SI Appendix*, Fig. S1*A*). The key cellular interactions varied by pathway: *RARRES2/CMKLR1* signaling occurred predominantly from fibroblasts to C1q Mphi (likely resident macrophages, top three differentially expressed genes, *C1QA, FOLR2,* and *C1QB*). *ANXA1/FPR2* signaling flowed from differentiated keratinocytes to both C1q and IL-1β Mphi (likely inflammatory Mphi, *IL1B, LGALS2,* and *OLR1*), while the *POMC/MC1R* pathway displayed more complex, multicellular interaction networks (Fig. 1 *A* and *B* and *SI Appendix*, Fig. S1*A*).

We focused subsequent analyses on the POMC/MC1R pathway, as while this signaling axis is well characterized in cutaneous biology for its roles in melanogenesis and UV responses (14, 15), its potential contribution to wound healing, particularly in chronic nonhealing wounds, remains largely unexplored (20). Analysis of transcript expression patterns revealed *POMC* to be broadly expressed across multiple cell types, with highest levels in fibroblasts and smooth muscle cells, while *MC1R* was predominantly detected in vascular endothelial cells, melanocytes, fibroblasts, and smooth muscle cells, with lower expression in keratinocytes (Fig. 1*C*). Cell–cell communication network analysis revealed extensive POMC–MC1R signaling with patterns that differed between healthy skin and DFU states. In healthy skin, keratinocytes and plasma cells emerged as dominant signal senders targeting primarily melanocyte receivers, with C1q Mphi, sweat glands, fibroblasts, and smooth muscle cells (SMC) serving as key mediators. During DFU healing, this network underwent significant reorganization: lymphatic endothelial cells and sweat glands became weak senders, while SMC, fibroblasts, and keratinocytes shifted to receiver roles. Notably, nonhealing DFU largely failed to demonstrate these adaptive changes in POMC–MC1R communication (Fig. 1*A* and *SI Appendix*, Fig. S1*B*).

Multiplex immunofluorescence was used to validate and extend scRNAseq results. Interestingly, we found a reduction in POMC+ cells in the ulcer bed, but not ulcer adjacent tissue in three categories of CWs, DFU, PU, and VLU relative to normal skin (NS; Fig. 1*D* and *SI Appendix*, Fig. S1 *D–E*). In contrast, MC1R+ cells demonstrated a trend of increasing number in both ulcer bed and adjacent tissue in comparison to healthy skin (Fig. 1*D*). POMC+ cells were predominantly podoplanin (PDPN)+ stromal cells (likely fibroblasts), tryptase+ mast cells, and basal keratinocytes (Fig. 1 *E* and *F*), while MC1R was primarily expressed by blood vessel endothelial cells and PDPN+ cells (Fig. 1 *G* and *H*).

Collectively, these results reveal dysregulation of the POMC–MC1R axis in human CWs, wherein diminished ligand expression coexists with elevated receptor expression. This pattern suggests that therapeutic intervention via exogenous MC1R ligand administration could potentially restore pathway equilibrium.

MC1R Is Required for Efficient Wound Repair. To establish the contribution of MC1R to wound healing, we generated 4 mm wounds to the dorsal skin of MC1Re/e mice, which harbor a nonfunctional receptor (ginger hair; C57Bl/6J background) and wildtype (black hair; C57Bl/6J) mice (Fig. 2*A*). We find that lack of functional MC1R profoundly impaired healing, with significantly delayed wound closure detectable at 1, 7, 10, and 14 d postinjury (DPI; at 7 DPI–MC1Re/e, 27.4 ± 2.1%; C57Bl/6J, 7.36 ± 0.83% of initial wound area; Fig. 2 *B–D*). Incomplete reepithelialization was evident in MC1Re/e wounds 7 DPI with presence of epithelial tongues and gap between them, in comparison to reformation of an intact epidermal layer in C57Bl/6J control wounds (Fig. 2*E*). This resulted in delayed scab loss (an indicator of complete reepithelialization), with 95.0% of MC1Re/e wounds retaining a scab at 7 DPI in comparison to 68.8% of wildtype control wounds (Fig. 2*F*). Wound bed administration of selective MC1R agonist BMS-470539 (MC1R Ag) had no effect on the wound healing response in MC1Re/e mice (Fig. 2 *B*, *C*, and *F*). Furthermore, abundant NETs were observed in 60% of MC1Re/e wounds, occupying an average of 5.6% of the wound area, while no NETs were observed in wildtype wounds (Fig. 2 *G* and *H*). This suggests a role for endogenous MC1R ligands in regulating NET formation. As murine wounds heal predominantly by contraction rather than reepithelialization, this may influence the degree of delayed closure observed in this model (21, 22). Nonetheless, the pronounced defects in reepithelialization and elevated NET burden highlight a key role for MC1R in regulating inflammatory and epithelial responses during skin repair, suggesting that MC1R is required for optimal skin repair.

CW Model Reproduces Hallmarks of the Human Pathology. Given that dysregulation of the POMC/MC1R axis was observed in human CWs (Fig. 1), we next sought to investigate whether MC1R contributes to impaired healing in a CW context. However, existing models of CWs suffer from significant limitations: Many resolve spontaneously and therefore fail to reflect the persistent, nonhealing nature of human pathology; others do not replicate key hallmarks such as advanced age or oxidative stress; some raise significant ethical concerns due to procedural severity; and not all models use genetically tractable species, limiting mechanistic insight (23–26).

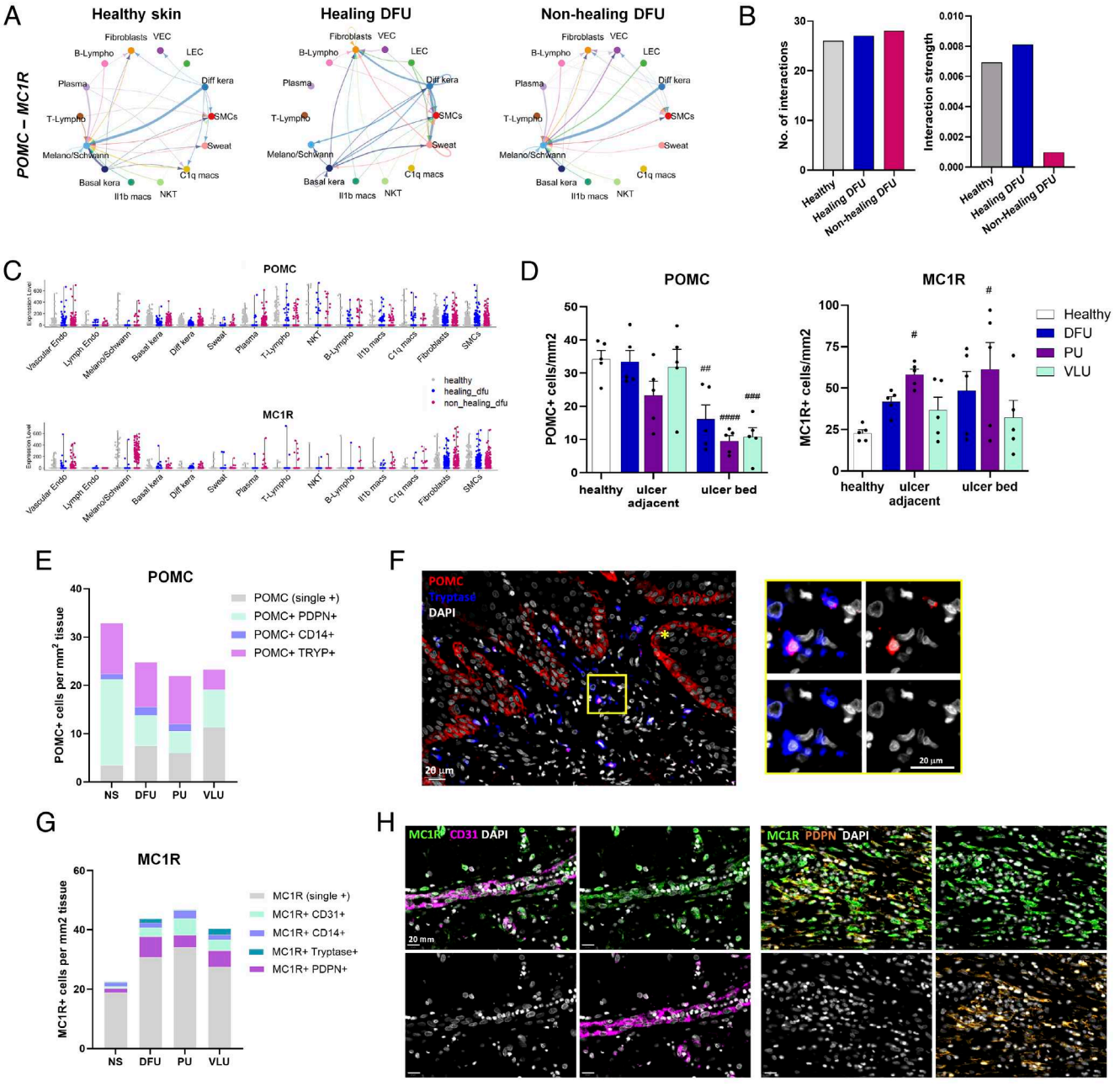

Fig. 1. Dysregulated POMC-MC1R axis in human chronic wounds. (*A*) Circle plots of inferred POMC-MC1R signalling networks in healthy human skin, healing diabetic foot ulcers (DFU) and non-healing DFU. Edge weight is proportional to the inferred interaction strength, with a thicker edge line indicating a stronger signal. Edges colours are consistent with the signalling source and arrows indicate signal direction. (*B*) Comparison of the total number of interactions and interaction strength for the POMC-MC1R ligand-receptor pair, illustrating reduced interaction strength in non-healing DFU in comparison to healthy skin and healing DFU. (*C*) Violin plots depicting POMC and MC1R transcript expression across cell types in healthy skin, healing and non-healing DFU. (*D*) Quantification of POMC+ and MC1R+ cells/mm2 in healthy dermis (n = 5), ulcer beds and ulcer adjacent dermis in PU (n = 5), DFU (n = 5) and VLU (n = 5). # $p < 0.05$, ## $p < 0.01$ relative to healthy group by two-way ANOVA with Bonferroni's multiple comparison test. (*E*) Stacked histogram illustrating the number and identity of POMC+ cells in healthy skin, DFU, PU and VLU. Quantification was performed across the entire biopsy (ulcer bed and adjacent tissue combined). (*F*) Representative multiplex immunofluorescence images illustrating POMC (red) stained basal keratinocytes (yellow star) and tryptase+ mast cells (blue; yellow box). (*G*) Stacked histogram illustrating the number and identity of MC1R+ cells in healthy skin, DFU, PU and VLU. Quantification was performed across the entire biopsy (ulcer bed and adjacent tissue combined). (*E*, *G*) Podoplanin (PDPN; stromal cells), CD14 (monocytes/macrophages), Tryptase (mast cells), CD31 (blood vessel endothelial cells). (*H*) Representative multiplex immunofluorescence images illustrating MC1R (green) expression in CD31 (magenta) blood vessels and PDPN (orange) stromal cells of chronic wounds. DAPI nuclear stain in white. Epi; epidermis. Inset with arrows marking blood vessels, BV. SMC, smooth muscle cells; Diff kera, differentiated keratinocytes; Lymph endo, lymphatic endothelial cells; Melano/Schwann, melanocytes/Schwann cells; NKT, natural killer T cells; Sweat/Seba, sweat/sebaceous glands. DFU, Diabetic Foot Ulcer; PU, Pressure Ulcer; VLU, Venous Leg Ulcer.

To overcome these challenges, we developed a humane and clinically relevant preclinical model suitable for testing interventions such as MC1R agonists and for dissecting mechanisms underpinning repair failure. While CWs have diverse underlying pathologies, including diabetes, immobility, and venous stasis, we aimed to establish a broadly applicable model rather than replicate a specific subtype (e.g., DFU, PU, VLU). Our approach was informed by two features common to most CWs: They predominantly affect people over 60 years of age and exhibit high wound bed oxidative stress. Building on previous models, we combined advanced age and induction of wound oxidative stress in our design [Fig. 3*A*; (23–26)].

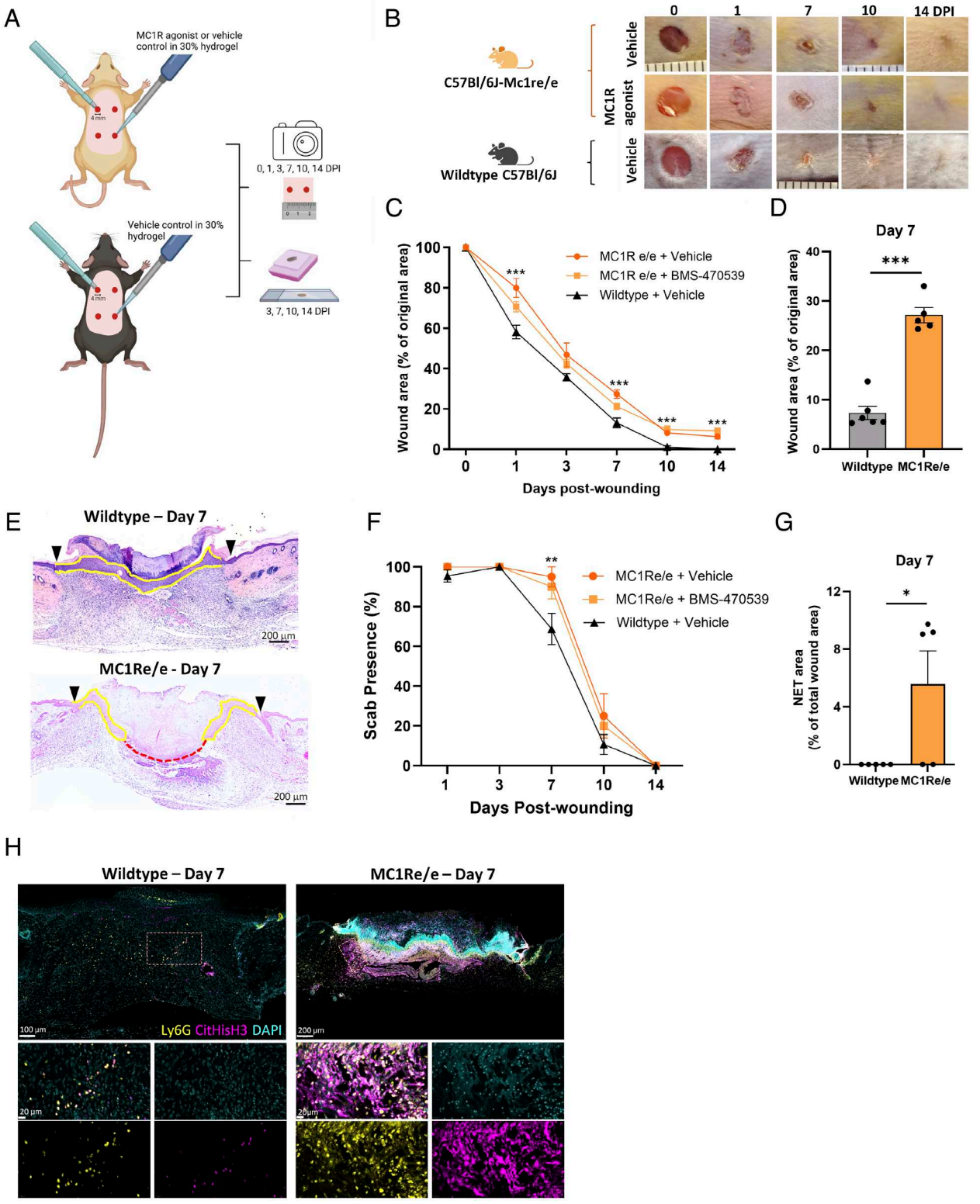

Fig. 2. MC1R is necessary for efficient wound healing. (*A*) Four 4 mm excisional wounds were made to the dorsal skin of MC1Re/e and C57Bl/6J mice. Vehicle (PBS) or MC1R agonist (BMS-470539) in 30% Pluronic hydrogel was administered topically immediately after wounding. Wound photos were taken at days 0, 1, 3, 7, 10, and 14 DPI and tissues harvested at 3, 7, 10, and 14 DPI. (*B*) Representative images of vehicle- and BMS-470539-treated wounds in MC1Re/e mice in comparison to C57Bl/6J vehicle-treated wounds. (*C*) Longitudinal quantification of wound areas in MC1Re/e and Wildtype mice at 1 to 14 DPI. (*D*) Wound area at 7 DPI in C57Bl/6J (n = 6 mice) and MC1Re/e mice (n = 5 mice). (*E*) Representative H&E-stained woundmid-sections at 7 DPI. Epithelial tongues (yellow) and epithelial gap (red dotted line) illustrate incomplete reepithelialization in MC1Re/e mouse wounds. (*F*) Percentage of wounds with scab present 1 to 14 DPI. (*G*) Quantification of NET area as percentage of total wound area 7 DPI. (*H*) Representative immunofluorescence images showing absence of NETs in wildtype wound and presence in MC1Re/e wound. NETs identified by coexpression of extracellular citrullinated Histone H3 (CitHisH3; magenta), DNA (DAPI, cyan), and Ly6G (yellow). (*C*, *D*, *F*, and *G*) Data are expressed as mean ± SEM. $^{**}P < 0.01$, $^{***}P < 0.001$ by two-way ANOVA with Bonferroni's multiple comparison test (*C* and *F*) or Student's unpaired *t* test (*D* and *G*) relative to wildtype wounds. (*C* and *F*) 5 MC1Re/e + vehicle, 5 MC1Re/e + BMS-470539 and 6 C57Bl/6J + vehicle-treated animals per group from 2 independent experiments. DPI, days postinjury.

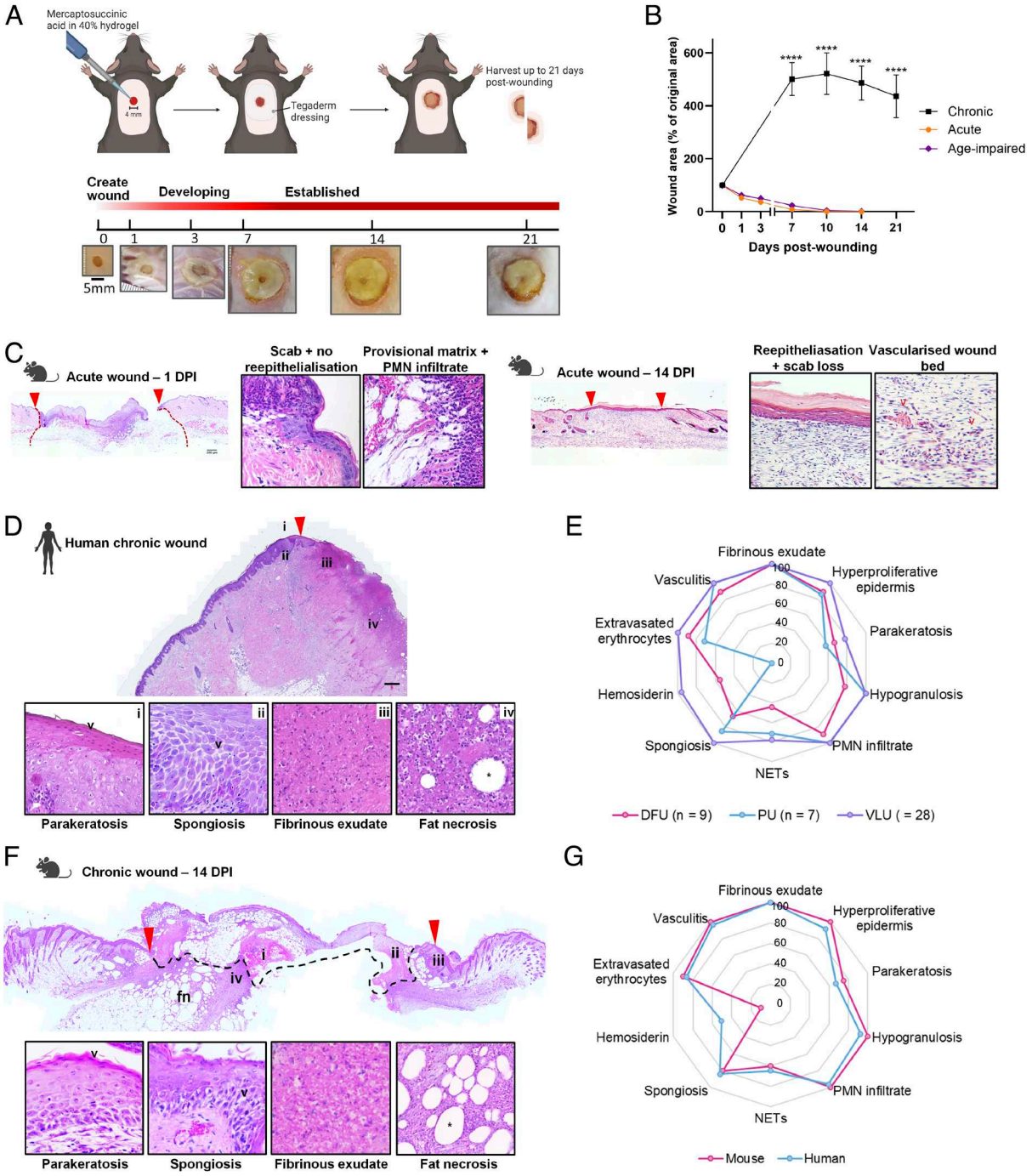

Fig. 3. CW model reproduces hallmarks of the human pathology. (*A*) *Top*—Schematic detailing the method used to create CWs. A single 4 mm excisional wound was made to the upper dorsal skin of 18 to 22-m-old C57Bl/6J mice. Mercaptosuccinic acid suspended in 40% Pluronic hydrogel was topically administered to the wound immediately after injury, followed by placement of a Tegaderm dressing and wound harvest up to 21 DPI. *Bottom*—Macroscopic photos showing CW development from 0 to 21 DPI. (*B*) Longitudinal macroscopic quantification of wound areas in acute (young 8-w-old mice; n = 8) and age-impaired (18 to 24-m-old mice; n = 8) healing versus chronic nonhealing wounds (n = 15 at 14 DPI, n = 8 at 7, 10, and 21 DPI). Data are expressed as mean ± SEM, ****$P < 0.0001$. (*C*) Representative low power field (lpf) mouse acute wound H&E sections at 1 DPI (*Left*) and 14 DPI (*Right*) with key histological features shown in high power field (hpf). n = 8 biological replicates. (*D*) Representative lpf human CW H&E section (n = 44 patients) with key histological features shown below in hpf. (*E*) Radar plot indicating mean prevalence (%) of key CW features in human DFU (n = 9), VLU (n = 28), and PU (n = 7). (*F*) Representative lpf mouse CW H&E sections at 14 DPI with key histological features shown below in hpf. n = 10 biological replicates from 3 independent experiments. (*G*) Radar plot indicating mean prevalence (%) of key features observed in human CWs (DFU, VLU, and PU, n = 44), in comparison to the murine preclinical CW model (n = 10). Red arrow heads indicate wound margins, * and fn indicates fat necrosis. DPI, days postinjury. *C*, *D*, and *F* wound margins denoted with red arrow.

A 4 mm excisional wound was made to the dorsal skin of aged mice, and topical glutathione peroxidase (GPx) inhibitor, mercaptosuccinic acid (MSA), was applied, following by a transparent Tegaderm dressing (Fig. 3*A*). The wounds expanded 5-fold into the surrounding tissue during the first 7 DPI and remained stable at this size throughout the experiment (Fig. 3 *A* and *B*). The tissue initially developed a macerated appearance (approx. 1 DPI), before progressing to produce exudate and slough, similar to human CWs (Fig. 3*A*). Wounds were well tolerated by the animals (*SI Appendix*, Fig. S2 *A–E*). Wound architecture was compared between the established acute excisional wound model (Fig. 3*C*), the new CW model (Fig. 3 *F* and *G*) and a cohort of 44 human CWs (28 VLU,

9 DFU, 7 PU; Fig. 3 *D* and *E* and *SI Appendix*, Table S1). During normal skin repair, at 1 DPI a scab has formed due to hemostasis, reepithelialization is not evident, provisional matrix has been deposited and a rich polymorphonuclear cell (PMN) infiltrate is present. By 14 DPI, reepithelialization is complete, the scab has been lost, few PMN remain, and the wound bed is well vascularized (Fig. 3*C*).

In human CWs, we found fibrinous exudate, hyperproliferative epidermis, PMN tinfiltrate, and vasculitis to be consistently present, identified in 86 to 100% of DFU, VLU, and PU (Fig. 3 *D* and *E*). Hypogranulosis (78 to 100%), extravasated erythrocytes (71 to 100%), parakeratosis (57 to 78%), and spongiosis (67 to 100%) were also common histomorphological features. Hemosiderin was the most variable feature, found in all VLU, 56% of DFU but none in PU, likely due to specific comorbidities including venous stasis most commonly found in VLU patients (Fig. 3 *D* and *E* and *SI Appendix*, Fig. S3*A*).

Our preclinical CW model showed excellent recapitulation of human CW hallmarks through macroscopic and histomorphological analysis (Fig. 3 *F* and *G*). Key features included fibrinous exudate (100%), extravasated erythrocytes (90%), and subcutaneous fat necrosis. Major epidermal disturbances included hyperproliferation (100%), spongiosis (80%), and parakeratosis (78%), with complete failure of wound reepithelialization.

While no animal model can fully recapitulate the complexity of human CWs, our approach captures several key features that are broadly conserved across CW categories. These include the use of aged animals, reflecting the human demographic most affected; induction of wound bed oxidative stress, a shared hallmark of CWs; and persistence of nonhealing wounds, rather than spontaneous resolution. In contrast to models relying on excessive procedural severity or nongenetically tractable species, our model is both humane and mechanistically informative, enabling testing of targeted therapies such as MC1R agonists in a controlled, reproducible setting. Having established a humane CW model that reflects key aspects of the human pathology, we next investigated whether MC1R-Ag administration could improve healing outcomes as a potential therapeutic approach.

MC1R Agonist Restores Healing in a Preclinical CW Model. In the clinic, nonhealing wounds are typically managed in the community, with dressing changes and basic wound debridement performed as part of standard wound care. Effective wound debridement is thought to partially stimulate healing, but in complex wounds, is typically insufficient to result in complete repair (12, 27). To assess a potential therapeutic intervention, we therefore debrided the wounds 7 DPI (Fig. 4 *A* and *B*). The selective MC1R agonist, BMS-470539 or vehicle-control were administered topically immediately after debridement and at each subsequent dressing change 3 and 5 d later (Fig. 4 *A* and *B*). Vehicle-treated debrided wounds mimicked the hallmarks of human CWs previously observed in nondebrided wounds (Fig. 3 *F* and *G*), including PMN infiltrate, fibrinous exudate, spongiosis, parakeratosis, a lack of wound vascularization and absence of reepithelialization (Fig. 4*B* and *SI Appendix*, Fig. S3*A*), while exhibiting a partial stimulation to healing, evident as a 30% reduction in wound area at 14 DPI (Fig. 4*C*). However, MC1R-Ag treatment following debridement rescued the healing response, with an additional 33% reduction in wound area over debridement alone by 14 DPI, rising to 68% at 21 DPI (Fig. 4 *B* and *C* and *SI Appendix*, Fig. S3*B*). Reepithelialization increased by 3.3-fold compared to vehicle controls (64.9% ± 10.4 vs. 19.9% ± 3.7; Fig. 4*D* and *SI Appendix*, Fig. S3*B*), as evidenced by formation of epithelial tongues (epidermis that has proliferated and migrated across the wound; *SI Appendix*, Fig. S3*B*), with complete reepithelialization achieved by 21 DPI. Incidence of histomorphological features, spongiosis, parakeratosis, and extravasated erythrocytes was reduced (*SI Appendix*, Fig. S3*D*). Presence of wound exudate was also reduced following MC1R-agonist treatment, with only 20% of wounds displaying visible exudate 14 DPI, reducing to 0% by 21 DPI (Fig. 4 *B* and *E*). In contrast, MC1Re/e CWs produced copious exudate both pre- and postwound debridement, such that 88% exhibited notable exudate 14 DPI in comparison to 56% of vehicle-treated wildtype wounds (Fig. 4 *B* and *E* and *SI Appendix*, Fig. S3 *C* and *E*). This improvement in wound condition coincided with a 1.6-fold reduction in neutrophil infiltration with MC1R agonist treatment and a 3.05-fold decrease in NET burden, while MC1Re/e wounds showed a 54% increase in neutrophils and 75% increase in NET burden relative to wildtype wounds (Fig. 4 *F*–*H*).

CWs in humans, including DFU, are characterized by poor angiogenesis, despite its essential role in effective cutaneous repair (10, 28). In our preclinical CW model, MC1R agonist promoted formation of a vascularized wound bed, increasing both blood vessel area and number, whereas MC1Re/e wounds exhibited a reduction in vessel number relative to wildtype mice (Fig. 4 *I* and *J*). Finally, stromal cell profiling revealed MC1R activation induced expansion of PDGFRα$^+$ cells (fibroblasts), including DPP4$^+$ and αSMA$^+$ subsets (Fig. 4*K* and *SI Appendix*, Fig. S3*F*). These populations are associated with tissue remodeling and vascular support, suggesting that MC1R signaling drives a shift in fibroblast phenotype toward one more conducive to repair (29). Notably, the reduction in PDPN$^+$, DLK1$^+$ fibroblasts, cells implicated in fibrotic responses (30, 31), suggests that MC1R activation suppresses profibrotic programs (Fig. 4*K*). This supports a model in which MC1R signaling modulates fibroblast fate and function to promote resolution of CWs through coordinated enhancement of vascularization and suppression of fibrosis.

To assess the broader relevance of these findings, we also evaluated MC1R agonist treatment in a diabetic version of the model, where impaired metabolic control is known to hinder wound healing (32). Although vehicle-treated wounds in this setting showed some spontaneous improvement at 14 DPI, the healing response remained limited. In contrast, MC1R agonist treatment significantly accelerated wound closure, reducing wound area to 44% by 12 DPI compared to 91% in controls (*SI Appendix*, Fig. S4 *A* and *B*). Histological analysis further revealed reduced presence of NETs, polymorphonuclear infiltrates, and extravasated erythrocytes in treated wounds (*SI Appendix*, Fig. S4*C*). Together, these data validate our CW model as a robust platform for therapeutic testing and demonstrate that MC1R agonism can rescue stalled healing.

Multifaceted Impact of MC1R Agonism On Acute Wound Repair. Having established MC1R agonist efficacy in CWs, we next examined its effects in acute wound healing. We administered MC1R-Ag or vehicle topically to 4 mm excisional wounds immediately after injury. Macroscopic analysis revealed accelerated wound closure in MC1R-Ag-treated wounds, with maximum differences in wound area noted at 3 and 7 DPI (Vehicle 7 DPI, 16.6 ± 3.8%; MC1R-Ag, 7 DPI, 4 ± 2.7% of original area Fig. 5 *A*–*C*). Key repair parameters were assessed, including epithelial tongue length and scab presence as measures of reepithelialization. Epithelial tongues were found to be significantly longer at 3 DPI with MC1R-Ag-treatment (Vehicle, 270 ± 19 μm; MC1R-Ag, 399 ± 22 μm *SI Appendix*, Fig. S5*A*). Using optical coherence tomography (OCT) imaging of the dynamic changes in epidermal thickness during wound healing, we demonstrate that harnessing MC1R results in earlier thickening of wound edge epidermis (peak

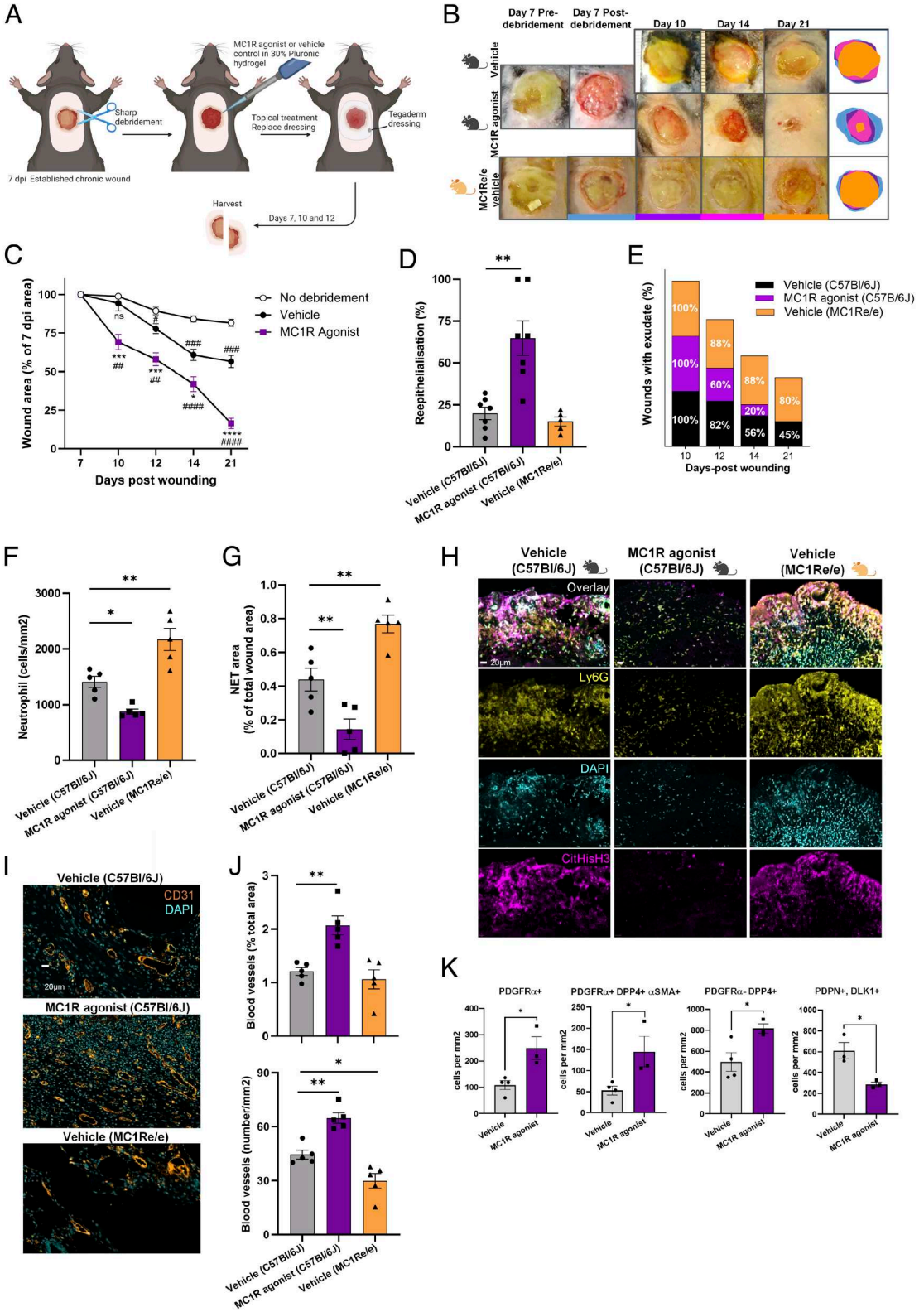

Fig. 4. MC1R agonist reinitiates healing in CWs. (*A*) Schematic of the CW protocol. Wounds were debrided at 7 DPI, with dressing changes and topical application of vehicle or MC1R agonist in 30% Pluronic hydrogel at 7, 10, and 12 DPI. Wounds were harvested at 14 and 21 DPI. (*B*) Representative images of CWs before and after debridement (7 DPI), and at 10, 12, 14, and 21 DPI following treatment. (*C*) Wound area quantification at 10 to 21 DPI, normalized to 7 DPI. two-way ANOVA with Tukey's multiple comparison test. # indicates comparison with No debridement. * indicates comparison between MC1R agonist and Vehicle. $P < 0.05$, * or #; $P < 0.01$, ##; $P < 0.001$, ***/###; $P < 0.0001$, ****/####. No debridement (n = 6), Vehicle (n = 8), MC1R agonist (n = 8). (*D*) Percentage reepithelialization at 14 DPI. (*E*) Prevalence of visible CW exudate with vehicle (n = 8), MC1R agonist (n = 8), MC1Re/e (n = 7) from three independent experiments. (*F*) Quantification of wound bed neutrophils at 14 DPI (*G*) NET area as percentage of total wound area at 14 DPI. (*F* and *G*) n = 5 wounds/group; 2 independent experiments). (*H*) Representative immunofluorescence images showing NETs (CitHisH3, magenta; DAPI, cyan; Ly6G, yellow) in vehicle-treated wounds and absence in MC1R agonist-treated wounds. (*I*) Representative images showing increased angiogenesis in MC1R agonist-treated wounds and reduced revascularization in MC1Re/e wounds. (*J*) Quantification of CD31+ blood vessels (n = 5 wounds/group; two independent experiments). (*K*) Quantification of wound stromal cell populations. (*D*, *F*, and *G*) one-way ANOVA. *$P < 0.05$; **$P < 0.01$; ***$P < 0.001$ with Dunnett's post hoc test. (*K*) Students unpaired *t* test, *$P < 0.05$.

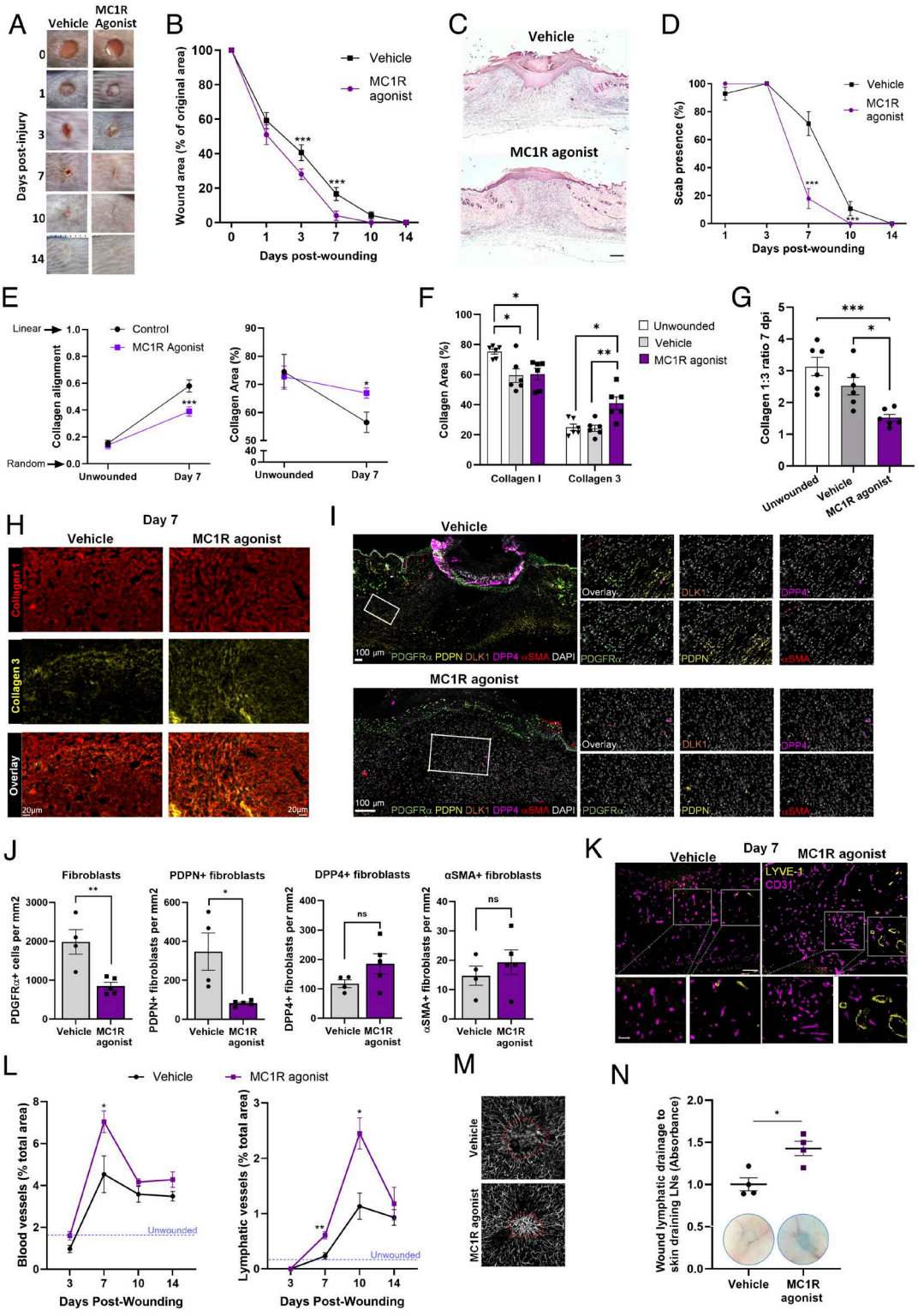

Fig. 5. Harnessing MC1R drives healing of acute cutaneous wounds. Four 4 mm excisional wounds were made to the dorsal skin of 8-wk-old C57Bl/6J mice. Vehicle (PBS) or MC1R agonist (BMS-470539) in 30% Pluronic hydrogel were administered topically immediately postwounding. (*A*) Representative macroscopic images and (*B*) wound area quantification 1 to 14 DPI. N = 7 mice per group, three independent experiments. (*C*) Representative H&E-stained wound mid-sections at 7 DPI illustrating scab loss and reduced wound size in MC1R agonist-treated wounds (5x, lpf). (*D*) Scab presence 1 to 14 DPI. N = 7 mice per group, three independent experiments. (*E*) Collagen alignment and area in unwounded skin and 7 DPI wounds stained with picrosirius red. N = 11 vehicle and 7 MC1R-Ag wounds per group. (*F*) Quantification of collagen 1 and 3 area in unwounded skin and 7 DPI wounds (n = 6 wounds per group). (*G*) Collagen 1:3 ratio in unwounded skin and 7 DPI (n = 6 wounds per group) (*H*) Representative immunostaining of collagen 1 (red) and 3 (yellow) at 7 DPI. (*I*) Representative fibroblast population immunostaining at 7 DPI. (*J*) Quantification of wound fibroblast populations (n = 4 vehicle wounds; n = 5 MC1R agonist wounds). (*K*) Representative CD31 (magenta) and LYVE-1 (yellow) immunostaining at 7 DPI (*L*) Quantification of $CD31^+$ (blood vessel) area and $LYVE\text{-}1^+$ (lymphatic vessel) area per hpf in wounds 3 to 14 DPI. n = 6 vehicle, n = 5 MC1R agonist from two independent experiments). Area in unwounded skin denoted by dotted blue line. (*M*) Optical coherence tomography (OCT) angiography at 7 DPI shows increased blood flow in MC1R agonist-treated wounds; the red line marks wound edge from structural OCT. (*N*) Representative images and quantification of skin-draining lymph nodes at 10 DPI following Evans blue injection into the wound bed, assessing lymphatic drainage in vehicle- vs MC1R agonist-treated wounds. Data are expressed as mean ± SEM. $*P < 0.05$, $**P < 0.01$, $***P < 0.001$ by two-way ANOVA with Bonferroni's multiple comparison test (*B, D, E, F,* and *L*), Student's unpaired *t* test (*J* and *N*), or one-way ANOVA (*G*) relative to vehicle-treated wounds. DPI; days postinjury.

at 3 DPI vs 5 DPI with vehicle-treatment), this was followed by a quicker reduction in epidermal thickness by 7 DPI (*SI Appendix*, Fig. S5 *B* and *C*). Since reepithelialization was completed earlier in MC1R-Ag-treated wounds, this resulted in reduced scab presence at 7 DPI (Vehicle, 71 ± 8.5%; MC1R-Ag, 18 ± 7% of wounds; Fig. 5*D*). We utilized an in vitro scratch wound assay to determine whether the observed effects of MC1R-Ag on reepithelialization could be through direct actions on epidermal keratinocytes. Indeed, MC1R-Ag accelerated keratinocyte scratch wound closure (*SI Appendix*, Fig. S5 *D–E*).

Physiological skin repair culminates in formation of a scar, which predominantly consists of linear bundles of collagen fibers, as opposed to normal dermis, which exhibits a basketweave appearance (1, 7). To quantify scarring, we measured collagen fiber orientation using a novel app, FIBRAL, and picrosirius red-stained sections. Unwounded skin exhibited abundant collagen with randomly oriented fibers corresponding with a low alignment index (0.152 ± 0.024; Fig. 5*E* and *SI Appendix*, Fig. S5*F*). In vehicle-treated day 7 wounds, collagen was laid down in a more linear fashion with a high alignment value, typical of a scar. Wound treatment with MC1R-Ag, however, resulted in collagen deposition with a more random orientation closer to unwounded dermal collagen organization, which equated to reduced alignment in comparison to vehicle-treated wounds (0.39 ± 0.036 MC1R-Ag vs 0.58 ± 0.045 vehicle; Fig. 5*E* and *SI Appendix*, Fig. S5*F*). We assessed collagen quantity, finding that MC1R-Ag also accelerated the rate of collagen deposition (66.9 ± 1.85% MC1R-Ag vs 56.5.2 ± 3.64% vehicle vs unwounded 74.5 ± 6.17%; Fig. 5*E* and *SI Appendix*, Fig. S5*F*). Using immunostaining, we also demonstrate that MC1R-Ag significantly increased wound collagen III deposition but did not alter collagen I levels, resulting in a decreased collagen I:III ratio (Fig. 5 *F–H*). This shift is consistent with improved scar quality, as excessive collagen I and highly aligned fibers are associated with fibrotic scarring, whereas higher collagen III content is linked to more regenerative, pliable tissue remodeling (33, 34). Thus, a downstream consequence of wound MC1R-Ag treatment is reduced scarring through improved collagen deposition quality and quantity. Building on these findings, we noted that MC1R-Ag administration reduced the fibroblast pool (PDGFRa+ cells), particularly PDPN+ fibroblasts, which are associated with fibrotic responses (Fig. 5 *I* and *J*) (30, 31). Similarly to CWs, this suggests that MC1R activation suppresses profibrotic programs.

Harnessing MC1R Drives Angiogenesis and Lymphangiogenesis at Sites of Cutaneous Repair. We next assessed the impact of harnessing MC1R on angiogenesis and lymphangiogenesis during acute wound repair. We find that wound treatment with MC1R-Ag profoundly enhances the angiogenic (155% at 7 DPI) and lymphangiogenic (216% at 10 DPI) responses with increased vessel density over vehicle-treated wounds (Fig. 5 *K* and *L*). We performed OCT angiography to verify that the CD31+ cell areas identified by immunofluorescence represented functional, perfused blood vessels. Indeed, OCT angiography revealed notable wound bed perfusion in the MC1R-Ag-treated group at 7 DPI (Fig. 5*M*). Using a microvascular endothelial cell tube formation assay, we tested whether MC1R-Ag directly promotes endothelial cell-driven wound vascularization. MC1R-Ag significantly enhanced in vitro angiogenesis parameters, including total mesh area, branching interval and total segment area (*SI Appendix*, Fig. S6 *B–E*). siRNA knockdown of MC1R confirmed that these effects of BMS-470539 are MC1R-dependent (*SI Appendix*, Fig. S6 *A* and *D*). To assess wound lymphatic function, we performed a drainage assay using Evans Blue dye injected into wounds and quantified its accumulation in skin-draining lymph nodes. MC1R-Ag treatment led to improved lymphatic drainage, consistent with the observed increase in lymphatic vessel area (Fig. 5*N*). Together, these findings demonstrate that BMS-470539 acts via endothelial cell MC1R to drive angiogenesis and lymphangiogenesis, resulting in improved wound bed blood supply and lymphatic function.

Conclusion. In summary, our work reveals a critical role for MC1R signaling in both acute and CW repair and identifies dysregulation of the MC1R/POMC axis as a shared pathological feature across DFU, VLU, and PU. Using a humane CW model that recapitulates key features of the human condition, we show that topical application of a selective MC1R agonist restores healing by reducing neutrophil infiltration and NET formation, enhancing vascularization and reepithelialization. Complementary studies in acute wounds demonstrate that MC1R agonism similarly improves vascularization and reduces scarring. MC1R agonists such as afamelanotide and dersimelagon have demonstrated favorable safety profiles in clinical trials for other indications, supporting the translational potential of this pathway (35–37). For CWs, a topical formulation applied at dressing changes could provide targeted activation while minimizing systemic exposure. Together, these findings uncover a key role for MC1R in skin repair and highlight its promise as a therapeutic target in both chronic and acute wound settings.

Materials and Methods

Human Tissue. Formalin-fixed paraffin embedded (FFPE) sections of human CWs were provided by NHS Lothian Tissue Bank (ethical approval: 15/ED/0094) with approval from the Tissue Governance Committee (SR612, SR1368, and SR736). Inclusion criteria were pressure ulcers, DFU, and venous leg ulcers from male and female donors. Exclusion criteria were patients with cancer and pressure ulcers from patients with diabetes. Prior to receipt, all samples were pseudonymized (Donor information provided in *SI Appendix*, Table S1).

Data Analysis of GSE165816. Public scRNA-seq data (Theocharidis et al., GSE165816) were reanalyzed in R (v4.2.2) with Seurat (v4.4). Data were normalized with SCTransform, filtered for quality, and clustered using PCA, UMAP, and shared nearest neighbor (SNN) analysis. Marker genes were used for annotation (*SI Appendix*).

POMC–MC1R Expression and Cell–Cell Communication. Low-abundance transcripts were pooled within clusters to generate normalized transcript per million (nTPM). Cell–cell communication was inferred using CellChat, which integrates scRNA-seq with ligand–receptor databases. Communication probabilities for POMC–MC1R were calculated using truncatedMean with permutation testing, yielding weighted interaction networks (*SI Appendix*).

Animals. All procedures were approved by the University of Edinburgh Local Ethical Review Committee and conducted under the UK Animals (Scientific Procedures) Act, 1986 (PPL PD3147DAB). C57Bl/6JCrl and MC1Re/e mice were bred under SPF conditions, housed 3 to 5 per cage, and monitored for health. Only healthy, procedure-naïve animals were used. Both acute and CW models were of moderate severity, with no deaths and <10% weight loss observed (see *SI Appendix* for husbandry and welfare monitoring).

Aging and Diabetes Models. Mice ≥12 mo were monitored weekly for weight, condition, and behavior, with veterinary review triggered by ≥10% weight loss or abnormality. Diabetes was induced by high-fat/high-sucrose diet followed by low-dose streptozotocin (40 mg/kg, i.p.), and confirmed by hyperglycemia (>13 mmol/L) (protocol in *SI Appendix*).

Wound Models. Acute wounds: Male and female mice (7 to 9 wk) received four 4-mm full-thickness dorsal wounds under isoflurane, with perioperative buprenorphine. Vehicle (PBS) or BMS-470539 was applied in 30% Pluronic hydrogel. Wounds were photographed and monitored up to 14 d.

CWs: Elderly mice (18 to 22 mo) received a single 4-mm excision treated with mercaptosuccinic acid (MSA) and covered with Tegaderm. At Day 7, wounds were debrided under anesthesia and treated with BMS-470539 or PBS. Mice were individually housed at 28 °C with softened diet and welfare monitored daily. Wound areas were measured by ImageJ (full methodology in *SI Appendix*).

Evans Blue Assay. To assess lymphatic drainage, Evans Blue dye (0.5% w/v) was injected into the wound bed 8 h before cull. Lymph nodes were harvested, dye extracted, and absorbance read at 610 nm (*SI Appendix*).

Histology and Immunostaining. Wounds were fixed in PFA, paraffin-embedded, and sectioned. Standard H&E and Picrosirius Red (for collagen) staining were performed. Immunohistochemistry used antigen retrieval, blocking, and multiplex immunofluorescence using Akoya OPAL reagents (*SI Appendix*, Table S3).

Image Analysis. Visiopharm software was used for segmentation and quantification of multiplex immunofluorescent images. Nuclear detection and phenotypic classification were applied within defined ROIs. Collagen density, neutrophil extracellular traps (NETs), and blood vessel areas were quantified. Collagen alignment was assessed using a custom MATLAB pipeline (FIBRAL) with Fourier analysis (*SI Appendix*).

Optical Coherence Tomography Angiography (OCTA). A prototype handheld OCTA device (University of Dundee) was used for in vivo imaging of wound healing and neovascularization. Anesthetised mice were scanned with a 200 kHz swept-source laser system, producing high-resolution 3D volumes for perfusion analysis (technical specifications in *SI Appendix*).

In Vitro Assays. Endothelial tube formation: HMEC-1 cells were transfected with siRNA control or MC1R-targeting oligonucleotides and seeded on Matrigel with/without BMS-470539. Tube length and branching were quantified using ImageJ. Keratinocyte scratch wound assay: HaCaT cells were wounded using the IncuCyte WoundMaker. Closure was monitored in real time for 48 h under 1% FBS with treatments applied and quantified as % wound confluence (*SI Appendix*).

Statistical Analysis. Student's *t* test, one-way and two-way ANOVA were performed using GraphPad Prism 10.0 software and detailed in the respective Figure legends.

Diagrams. Biorender was used to create the schematics in Figs. 2–5.

Data, Materials, and Software Availability. All data underlying the figures and analyses reported in the manuscript have been deposited in Figshare (https://figshare.com/s/ab023a159334d5b81b35). Data comprising Fig. 1 *A–C* were derived from analysis of GSE165816.

ACKNOWLEDGMENTS. We acknowledge the support of the University of Edinburgh histological services and BVS (Bioresearch and Veterinary Services), especially Dr Nacho Vinuela-Fernandez for assistance with animal studies. We thank Professor Ian Jackson for providing the MC1Re/e mouse line and Dr Andrew Tambyraja and Professor Keith Harding for helpful insights into CWs from a clinical perspective. We thank Dr Matthieu Vermeren (CALM services) for microscopy input. This work has made use of the resources provided by the Edinburgh Compute and Data Facility (ECDF). Sincere thanks also go to Prof David Dockrell, Prof Julia Dorin, and Prof Sarah Walmsley for mentorship. This work was funded by a Sir Henry Dale Fellowship (202581/Z/16/Z), Elizabeth Blackwell Early Career Fellowship (Wellcome ISSF), and a University of Edinburgh Chancellors Fellowship awarded to J.L.C. H.R.R. was supported with a Chancellors Fellowship PhD Studentship. Work in MC lab was funded by an EPSRC New Investigator grant EP/S019847/1, and C.A.B. is funded by a Carnegie Trust for Scotland PhD studentship.

Author affiliations: [a]Centre for Inflammation Research, Institute for Regeneration and Repair, University of Edinburgh, Edinburgh EH16 4UU, United Kingdom; [b]Biochemical Pharmacology, William Harvey Research Institute, Barts and the London School of Medicine and Dentistry, London EC1M 6BQ, United Kingdom; [c]Centre for Cardiovascular Research, The Queen's Medical Research Institute, University of Edinburgh, Edinburgh EH16 4TJ, United Kingdom; [d]School of Science and Engineering, Fulton Building, University of Dundee, Dundee DD1 4HN, United Kingdom; [e]Institute of Mechanical, Process and Energy Engineering, School of Engineering and Physical Sciences, Heriot-Watt University, Edinburgh EH14 4AS, United Kingdom; [f]Centre for Regenerative Medicine, Institute for Regeneration and Repair, University of Edinburgh, Edinburgh EH16 4UU, United Kingdom; and [g]Department of Pathology, Western General Hospital, Edinburgh EH4 2XU, United Kingdom

1. J. L. Cash, P. Martin, Myeloid cells in cutaneous wound repair. *Microbiol. Spectr.* **4**, 17 (2016).
2. S. A. Eming, T. A. Wynn, P. Martin, Inflammation and metabolism in tissue repair and regeneration. *Science.* **356**, 1026–1030 (2017).
3. C. K. Sen *et al.*, Human skin wounds: A major and snowballing threat to public health and the economy. *Wound Repair Regen.* **17**, 763–771 (2009).
4. T. Montero-Melendez *et al.*, Therapeutic senescence via GPCR activation in synovial fibroblasts facilitates resolution of arthritis. *Nat. Commun.* **11**, 745 (2020).
5. M. W. Alnouri *et al.*, SPMs exert anti-inflammatory and pro-resolving effects through positive allosteric modulation of the prostaglandin EP4 receptor. *Proc. Natl. Acad. Sci. U.S.A.* **121**, e2407130121 (2024).
6. M. Yi, J. E. Schnitzer, Impaired tumor growth, metastasis, angiogenesis and wound healing in annexin A1-null mice. *Proc. Natl. Acad. Sci. U.S.A.* **106**, 17886–17891 (2009).
7. J. L. Cash *et al.*, Resolution mediator chemerin15 reprograms the wound microenvironment to promote repair and reduce scarring. *Curr. Biol.* **24**, 1406–1414 (2014).
8. M. Quiros *et al.*, Resolvin E1 is a pro-repair molecule that promotes intestinal epithelial wound healing. *Proc. Natl. Acad. Sci. U.S.A.* **117**, 9477–82 (2020).
9. M. Olsson *et al.*, The humanistic and economic burden of chronic wounds: A systematic review: The burden of chronic wounds. *Wound Rep. Reg.* **27**, 114–125 (2019).
10. R. G. Frykberg, J. Banks, Challenges in the treatment of chronic wounds. *Adv. Wound Care* **4**, 560–582 (2015).
11. S. R. Nussbaum *et al.*, An economic evaluation of the impact, cost, and Medicare policy implications of chronic nonhealing wounds. *Value Health* **21**, 27–32 (2018).
12. J. F. Guest, G. W. Fuller, P. Vowden, Cohort study evaluating the burden of wounds to the UK's National Health Service in 2017/2018: Update from 2012/2013. *BMJ Open* **10**, e045253 (2020).
13. C. K. Sen, Human Wound and Its Burden: Updated 2020 Compendium of Estimates. *Adv. Wound Care.* **10**, 281–292 (2021).
14. P. Valverde, E. Healy, I. Jackson, J. L. Rees, A. J. Thody, Variants of the melanocyte–stimulating hormone receptor gene are associated with red hair and fair skin in humans. *Nat. Genet.* **11**, 328–330 (1995Nov).
15. J. S. Palmer *et al.*, Melanocortin-1 receptor polymorphisms and risk of melanoma: Is the association explained solely by pigmentation phenotype?. *Am. J. Hum. Genet.* **66**, 176–186 (2000).
16. G. Leoni *et al.*, The melanocortin MC1 receptor agonist BMS-470539 inhibits leucocyte trafficking in the inflamed vasculature: Melanocortins control vascular inflammation. *British J. Pharmacol.* **160**, 171–80 (2010).
17. J. Panezai, T. E. Dyke, Resolution of inflammation: Intervention strategies and future applications. *Toxicol. Appl. Pharmacol.* **449**, 116089 (2022).
18. G. Theocharidis *et al.*, Single cell transcriptomic landscape of diabetic foot ulcers. *Nat. Commun.* **13**, 181 (2022).
19. S. Jin *et al.*, Inference and analysis of cell-cell communication using Cell Chat. *Nat. Commun.* **12**, 1088 (2021).
20. L. A. Muffley, K. Q. Zhu, L. H. Engrav, N. S. Gibran, A. M. Hocking, Spatial and temporal localization of the melanocortin 1 receptor and its ligand α–melanocyte-stimulating hormone during cutaneous wound repair. *J. Histochem. Cytochem.* **59**, 278–288 (2011).
21. L. Chen, R. Mirza, Y. Kwon, L. A. DiPietro, T. J. Koh, The murine excisional wound model: Contraction revisited. *Wound Repair Regen.* **23**, 874–877 (2015).
22. H. D. Zomer, A. G. Trentin, Skin wound healing in humans and mice: Challenges in translational research. *J. Dermatol. Sci.* **90**, 3–12 (2018).
23. R. Nunan, K. G. Harding, P. Martin, Clinical challenges of chronic wounds: Searching for an optimal animal model to recapitulate their complexity. *Disease Models Mech.* **7**, 1205–1213 (2014).
24. J. K. Zindle, E. Wolinsky, K. M. Bogie, A review of animal models from 2015 to 2020 for preclinical chronic wounds relevant to human health. *J. Tissue Viability* **30**, 291–300 (2021).
25. S. Dhall *et al.*, A novel model of chronic wounds: Importance of redox imbalance and biofilm-forming bacteria for establishment of chronicity. *PLoS ONE* **9**, e109848 (2014).
26. S. Dhall *et al.*, Generating and reversing chronic wounds in diabetic mice by manipulating wound redox parameters. *J. Diabetes Res.* **2014**, 1–18 (2014).
27. J. R. Wilcox, M. J. Carter, S. Covington, Frequency of debridements and time to heal: A retrospective cohort study of 312 744 wounds. *JAMA Dermatol.* **149**, 1050 (2013).
28. F. Renò, M. Sabbatini, Breaking a Vicious Circle: Lymphangiogenesis as a New Therapeutic Target in Wound Healing. *Biomedicines.* **11**, 656 (2023).
29. C. A. Worthen *et al.*, CD26 identifies a subpopulation of fibroblasts that produce the majority of collagen during wound healing in human skin. *J. Invest. Dermatol.* **140**, 2515–2524.e3 (2020).
30. B. Nazari *et al.*, Altered dermal fibroblasts in systemic sclerosis display podoplanin and CD90. *Am. J. Pathol.* **186**, 2650–2664 (2016).
31. F. Zeng *et al.*, Role and mechanism of CD90+ fibroblasts in inflammatory diseases and malignant tumors. *Mol. Med.* **29**, 20 (2023).
32. T. M. Bauer *et al.*, Mechanisms of impaired wound healing in type 2 diabetes: the role of epigenetic factors. *Arterioscler. Thromb. Vasc. Biol.* **45**, 321446 (2025).
33. L. Lin-Hui *et al.*, Recombinant human collagen type III improves hypertrophic scarring by regulating the ratio of type I/III collagen. *J. Burn Care Res.* **45**, 1269–1273 (2024).
34. D. Singh, V. Rai, D. K. Agrawal, Regulation of collagen I and collagen III in tissue injury and regeneration. *Cardiol. Cardiovasc. Med.* **7**, 5–16 (2023).
35. M. Balwani *et al.*, Dersimelagon in erythropoietic protoporphyrias. *N Engl. J. Med.* **388**, 1376–1385 (2023).
36. R. K. Leaf *et al.*, Afamelanotide for treatment of the protoporphyrias: impact on quality of life and laboratory parameters in a US Cohort. *eLife* **14**, 689 (2024).
37. M. Kondo *et al.*, Dersimelagon, a novel oral melanocortin 1 receptor agonist, demonstrates disease-modifying effects in preclinical models of systemic sclerosis. *Arthritis Res Ther.* **24**, 210 (2022).